A proton detector for energies from 2 MeV to 20 MeV

Marine Ruffenach, Sebastien Bourdarie, Julien Mekki, Didier Falguère, Jean-Roch Vaillé, Jérôme Carron

A proton detector for energies from 2MeV to 20MeV

M. Ruffenach, S. Bourdarie, J. Mekki, D. Falguère, J. R. Vaillé, and J. Carron

***Abstract*—CNES and ONERA have developed a radiation monitor ICARE-NG to measure protons and electrons in radiation belts. This instrument is able to measure a wide range of energy for protons and electrons, but no measurements of few MeV protons are performed. The objective of this study is to extend capabilities of this radiation monitor by adding a low energy proton sensor. In this article the design of a detector for low energy protons compatible with the ICARE-NG instrument is presented. Response functions for protons and electrons of the low energy proton detector are calculated using Monte-Carlo simulations. The calculation of predicted count rates of particles using the AP-8 and AE-8 models will be performed.**

***Index Terms*—Geant4, Monte-Carlo simulations, proton, radiation belts, radiation monitor, response function, space environment.**

I. Introduction

Due to the magnetic field of the Earth, protons and electrons are trapped in a restricted region of the magnetosphere and constitute radiation belts [1]. A good knowledge of these regions is mandatory to prevent damages on satellites or even their loss [2]. While a bunch of measurements of proton flux with energies greater than 10 MeV are available, in-situ measurements of 1-10 MeV protons are not common. The challenge to have good measurements of low energy protons is to accurately discriminate protons with energy of a few MeV to protons with energy of several tens of MeV, and to energetic electrons. Such monitors have already been developed: MEPED [3] [4], LPT [5], SST [6] and RBSPICE [7]. The aim of this study is to design a sensor of low energy protons compatible with the existing ICARE-NG instrument which flew over several missions as JASON-2 [8] and SAC-D [9]. Valid proton energy range measured by ICARE-NG on JASON-2 and SAC-D is from 12.8 MeV to 190 MeV. Such a new sensor will extend this energy range down to 2 MeV protons.

In section II, a brief presentation of the ICARE-NG instrument as well as the geometry of the detector of low energy protons are given. In section III the modelling of the instrument is described. In particular, Monte-Carlo simulations are outlined. Section IV focuses on numerical results of response functions of the detector and the modelling of predicted count rates of particles. Finally, conclusions are given in section V.

Manuscript submitted April 10, 2019.

This work was conducted as part of a co-financing of doctoral thesis research CNES N° 17054 - ONERA N° 9218.

M. Ruffenach, S. Bourdarie and D. Falguère are with The French Aerospace Lab/Département Physique Instrumentation Environnement et Espace, ONERA, 31055 Toulouse, France (e-mail: marine.ruffenach@onera.fr).

J. Mekki and J. Carron are with CNES, 31401 Toulouse, France.

J.R. Vaillé is with IES – UMR UM/CNRS 5214, Université de Montpellier, 34097 Montpellier, France.

II. The instrument's geometry

The geometry of the low energy proton detector has to satisfy several objectives: (1) an accurate discrimination of ionizing particles in a mixed field must be guaranteed, (2) it must be compatible with the existing ICARE-NG electronic design, and (3) it must be compatible with the actual mechanical design of ICARE-NG. Satisfying the second constraint imposes to implement a sensor based on solid state detectors with coincidence and anti-coincidence modes and to measure energy deposition in the 0-10 MeV range approximatively. The third objective means that the size of the sensor is limited in term of dimension and weight. The first objective is much more challenging: for example, in a 700 µm thick silicon diode a 1-MeV proton can deposit the same amount of energy than a 100-MeV proton or a 1-MeV electron. So, the first challenge to face is to reduce the contribution of electrons and high energy protons in order to get accurate measurements of low energy protons. To reduce the contribution of electrons and high energy protons the shielding is made of tungsten. However, the Bremsstrahlung depends on the square of the atomic number of the element so the tungsten fosters this phenomenon. The Bremsstrahlung depends also on the energy of the incident electron so to reduce this effect aluminum is added on both sides of the tungsten to reduce the energy of electrons before they reach the tungsten. At the main entrance of the detector, a samarium-cobalt magnet is used to deflect the major part of electrons before they reach the first silicon diode. Because protons are heavier, they are not affected in the energy range of interest (few MeV). The magnet is described in section III. Aluminum baffles are used to attenuate the scattering of particles in the collimator. To improve measurement quality, two silicon diodes are used to collimate particles. Moreover, diameters of diodes are chosen so as to reduce the contribution of particles coming from the sides of the instrument. In particular, the diameter of the first diode is lower than the one of the second diode. Last but not least, the instrument has to be compatible with the ICARE-NG instrument for which the complete description can be found in [8]. The ICARE-NG

instrument consists of three detector heads (A, B, and C). Both sensors A and C are set to measure protons while the Head-B measures electrons. Particle fluxes for electrons from 250keV to 3.2MeV and for protons from 12.8MeV to 190MeV are obtained. The goal now is to be able to implement either the actual Head-C of ICARE-NG or the new low energy proton sensor with no impact on electronic or mechanical design. This leads to other constraints for the geometry of the low energy proton detector. The positions of diodes in the new detector's head have to be roughly the same than in the Head-C. Also, the volume of the new head is limited by other heads so the thickness of the shielding must be the same as for the Head-C. As the Head-B detects electrons, the low energy proton head has to not interact with other heads, especially due to the magnetic field produced by the magnet. A steel strapping is used to confine the magnetic field inside the head. An illustration of the geometry of the low energy proton head taking into accounts all the constraints discussed above is shown in Fig. 1.

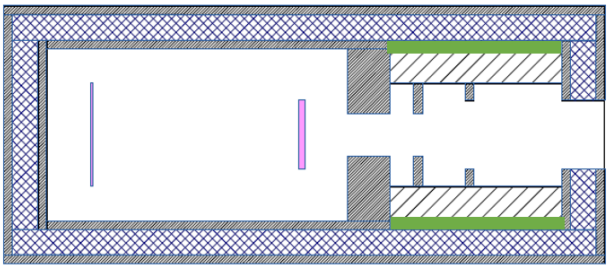

Fig. 1. Cross-section of the geometry of the low energy proton detector. Aluminum is represented in grey, tungsten in blue, diodes in pink, steel strapping in green, and pieces of samarium-cobalt in hatched areas.

The front silicon diode of 700µm thick has a sensitive area of 50mm² while the back silicon diode of 300µm thick has a sensitive area of 113mm².

III. The Modeling of the Instrument

A. Magnetic field calculation

The magnet is composed of two samarium-cobalt pieces so that the magnetic field is oriented diametrically. The height of the samarium-cobalt magnet is a compromise between the total volume of the detector and the deflection of electrons.

The magnetic field of the samarium-cobalt magnet is calculated using PS-PERMAG software [10]. The vertical cross-section of this calculation is presented in Fig. 2.

Between the two pieces, the magnetic field is approximately uniform. At the center the magnetic field is equal to 0.36T. These calculations do not take into account the steel strapping which will increase the intensity of the magnetic field between the two pieces and confine the magnetic field inside the head. Results of this magnetic field calculation are used in Monte-Carlo simulations to calculate the response of the low energy proton detector.

B. Monte-Carlo simulations

Response functions of protons and electrons in anti-coincidence and coincidence modes of the low energy proton

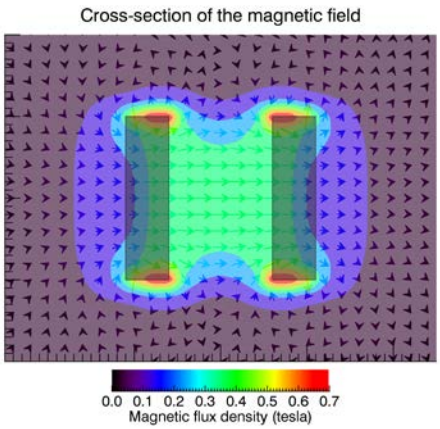

Fig. 2. Vertical cross-section of the magnetic field produced by the magnet.

head are computing from Monte-Carlo simulations based on the GEANT-4 ("GEometry ANd tracking") toolkit [11] [12]. The geometry of the low energy proton detector is drawn and translated into GEANT-4 using FASTRAD Software [13]. In these simulations a spherical source with a radius equals to $4.5cm$ is assumed with a cosine-law angular distribution for velocity vector directions [14]. Five million of tries are performed per incident energy. The efficiency of the detector is simulated by calculating the geometric factor, GEF, which is obtained from the ratio between the number of particles detected per channel over the total number of particles launched per incident energy. Its expression is given in (1) and calculated using [14] and [15].

$$GEF = 4\pi^2 R^2 \frac{N_{det}}{N_{Total}} \quad (1)$$

where R is the radius of the source.

At the entrance of the detector, an aluminum foil of 50µm is added for Monte-Carlo simulations to take into account the MLI (Multi-Layer Insulation) of the satellite which will cover the instrument.

IV. Numerical Results

A. Response functions

Proton response functions in anti-coincidence and coincidence modes are shown in Fig. 3 and in Fig. 4.

In Fig. 3 two regions can be highlighted: protons with an incident energy lower than 10MeV and protons with an incident energy higher than 65MeV. The first part is attributed to protons which depose all their energy in the front diode of the detector. The second part is attributed to protons which cross the shielding before reaching the front diode.

In Fig. 4 the response function indicates two regimes: protons with energies lower than 65MeV which come from the aperture of the detector and depose energy in the two diodes, and protons with incident energies higher than 65MeV and cross the shielding before reaching the two diodes.

With Fig. 3 and Fig. 4, 2-20MeV protons are measured thanks to anti-coincidence and coincidence modes. In the two cases, high energy protons cross the shielding and are detected with a higher geometric factor than the one of 2-20MeV energy protons.

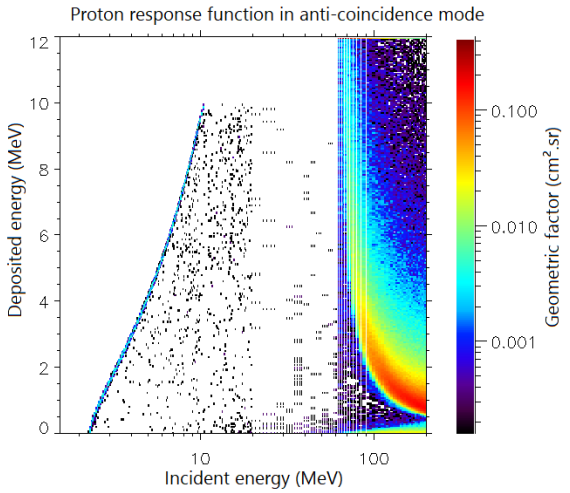

Fig. 3. Proton response function in anti-coincidence mode. Geometric factor (cm².sr) in incident energy (x-axis)-deposited energy (y-axis) map.

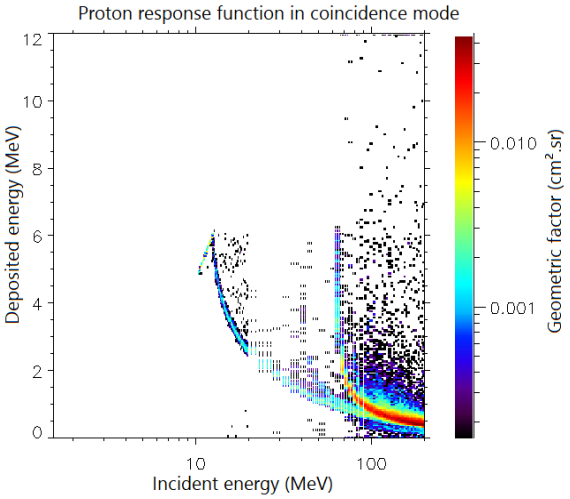

Fig. 4. Proton response function in coincidence mode. Geometric factor (cm².sr) in incident energy (x-axis)-deposited energy (y-axis) map.

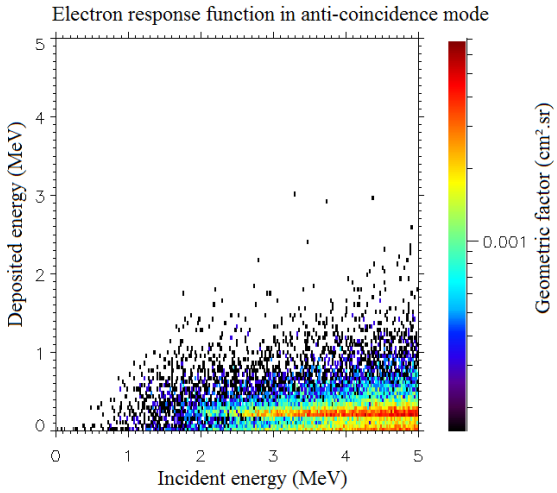

Fig. 5. Electron response function in anti-coincidence mode. Geometric factor (cm².sr) in incident energy (x-axis)-deposited energy (y-axis) map.

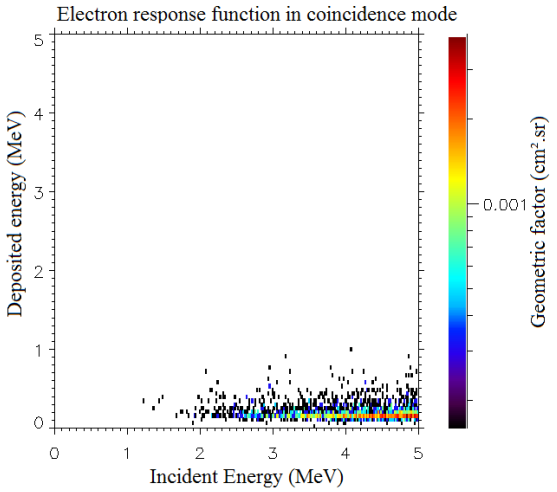

Fig. 6. Electron response function in coincidence mode. Geometric factor (cm².sr) in incident energy (x-axis)-deposited energy (y-axis) map.

Simulations were performed using the same number of particles for all incident energies. Nevertheless, in space fluxes of particles depend on the energy. Flux models will be taken into account in the subsection IV. B. to investigate the relative contribution of 2-20 MeV protons and higher energies.

Electron response functions in anti-coincidence and coincidence modes are shown in Fig. 5 and Fig. 6.

In Fig. 5 some electrons are detected in anti-coincidence mode. More precisely, they are mostly photons produced by the Bremsstrahlung. If we compare with the geometric factor of protons in anti-coincidence, the one in the case of electrons is much lower. This is due to the magnet which deflects the major part of electrons. In addition, electrons deposit energies less than 2MeV so some electrons will be detected only in the first channels.

In Fig. 6 few electrons are detected in coincidence mode but with a very low geometric factor. Furthermore, for all these simulations (protons and electrons) no threshold has been taken into consideration to filter out low energy depositions (and electronic noise by the way).

With a threshold set at 0.5MeV for example, which is the case for the Head-A of ICARE-NG, few electrons would be detectable only in anti-coincidence mode.

These response functions characterize the efficiency of the sensor to measure protons and electrons, but do not take into consideration particles distribution. In subsection IV. B, response functions and fluxes of particles are used to simulate particles' counts that will be returned by the instrument.

B. The modeling of calculated counts of particles

Fluxes of particles depend strongly on the satellite's location in the radiation belts. To take into account the response functions of the detector and particle distributions, expected count rates for each channel are computed. The expression of count rates for a given deposited energy channel is provided in (2) and extracted from [16].

$$C = \int_{\alpha_{local}} \int_{E} flux(E, \alpha_{local}) \times Map(E, \alpha_{local}) \times dE d\alpha_{local} \quad (2)$$

where $Map(E, \alpha_{local})$ and $Flux(E, \alpha_{local})$ are respectively the geometric factor and the unidirectional differential flux at a given incident energy and local pitch-angle. In a first step,

particle fluxes will be considered isotropic at spacecraft locations so response functions computed from an isotropic source will be adopted. After [17] [18] and [19] a correction factor is applied to electron fluxes with energies greater than 800 keV at L<2.5 returned by AE-8 model [20] [21]: AE-8 fluxes are divided by a factor 100 for $L < 2.5$ and for energies greater than 800 keV. Count rates are calculated for all deposited energy channels along the magnetic equator. Results obtained for the anti-coincidence mode are shown in Fig. 7.

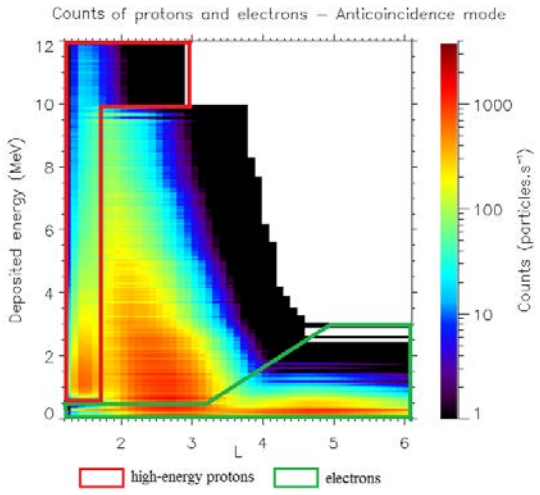

Fig. 7. Count rates of particles in McIlwain L-parameter (x-axis)-deposited energy (y-axis) map for the low energy proton detector in anti-coincidence mode.

Count rates obtained in Fig. 7 exhibit three regions. The first one with a red contour indicates count rates dominated by protons with energies greater than 65 MeV. The second one represented in green points out count rates dominated by energetic electrons. For the third one (with no specific contour) 2-20MeV protons dominate count rates. Clearly, the adopted sensor geometry allows discriminating 2-20 MeV protons accurately in a large radiation belt domain, and particularly allows sampling the pic flux. For $L < 1.7$ high energy protons dominate count rates but their contribution cannot be easily removed since these protons cross the aluminum-tungsten shielding. To limit even more their contribution the shielding has to be thicker. But design constrains to fit with the actual ICARE-NG radiation monitor, make it difficult to increase again mass and volume of the low energy proton sensor.

In the final version of the paper, results for the coincidence mode will be discussed. Also, count rates of low-energy protons will be calculated by taking into account the pointing direction of the monitor according to the magnetic field.

V. Conclusion

A new sensor of low energy protons has been designed. This sensor is compatible with the ICARE-NG instrument and can replace the Head-C according to the needs. Monte-Carlo simulations have been performed to calculate response functions of the sensor. By combining response functions calculated with GEANT4 and particle fluxes given by AP-8 and AE-8 models, predicted count rates have been calculated. Sensor performances indicate that the detector is sensitive to 2-20MeV protons for $1.7 < L < 3.5$.

References

[1] S. Bourdarie, and D. Boscher, “Space radiation environment”, Space Radiation Environment and its Effects on Spacecraft Components and Systems SREC04, Cépaduès Editions, 2004.

[2] D. N. Baker, ‘The occurrence of operational anomalies in spacecraft and their relationship to space weather’, IEEE Transactions on Plasma Science, vol. 28, no. 6, pp. 2007–2016, Dec. 2000.

[3] D. S. Evans, and M. S. Greer, “Polar Orbiting Environmental Satellite Space Environment Monitor - 2: Instrument Descriptions and Archive Data Documentation”, NOAA Technical Memorandum, Space Environment Center, Boulder, Colorado, Dec. 2000.

[4] K. Yando, R. M. Millan, J. C. Green, and D. S. Evans, “A Monte Carlo simulation of the NOAA POES Medium Energy Proton and Electron Detector instrument”, Journal of Geophysical Research, vol. 116, A10231, doi:10.1029/2011JA016671, 2011.

[5] Y. Sasaki et al., “Technical data acquisition equipment for GOSAT”, International Cosmic Ray Conference Proceedings, Mexico, 2007.

[6] J.L. Burch, and V. Angelopoulos, “The THEMIS Mission,” Springer, Space Science Reviews Volume 141, Issues 1–4, 2008.

[7] D.G. Mitchell et al., “Radiation Belt Storm Probes Ion Composition Experiment (RBSPICE)”, N. Fox, and J.L. Burch, The Van Allen Probes Mission. Springer, Boston, 2013.

[8] D. Boscher et al., “In Flight Measurements of Radiation Environment on Board the French Satellite JASON-2”, IEEE Transactions on Nuclear Science, vol. 58, no. 3, pp. 916–922, Jun. 2011.

[9] D. Boscher et al., “In-Flight Measurements of Radiation Environment on Board the Argentinean Satellite SAC-D”, IEEE Transactions on Nuclear Science, vol. 61, no. 6, pp. 3395–3400, Dec. 2014.

[10] “PS-PERMAG Software for Calculating Permanent Magnetic Fields”, Permagsoft [Online]. Available: http://www.permagsoft.com/english/Software/software.html.

[11] S. Agostinelli et al., “Geant4—a simulation toolkit”, Nuclear Instruments and Methods in Physics Research Section A: Accelerators, Spectrometers, Detectors and Associated Equipment, vol. 506, no. 3, pp. 250–303, Jul. 2003.

[12] J. Allison et al., “Geant4 developments and applications,” IEEE Trans. Nucl. Sci., vol. 53, no. 1, pp. 270–278, Feb. 2006.

[13] “FASTRAD Software – The 3D CAD Tool For Radiation Shielding Analysis”, TRAD [Online]. Available: https://www.fastrad.net/.

[14] G. Santin. “Normalisation Modelling Sources. Geant4”. [Online]. Available: http://geant4.in2p3.fr/2007/prog/GiovanniSantin/GSantin_Geant4_Paris07_Normalisation_v07.pdf

[15] J. D. Sullivan, “Geometric factor and directional response of single and multi-element particle telescopes’, Nuclear Instruments and Methods”, vol. 95, no. 1, pp. 5–11, Aug. 1971.

[16] M. Ruffenach et al., “Proton radiation belts anisotropy as seen by ICARE-NG Head-A,” IEEE Transactions on Nuclear Science, 2019.

[17] D. Boscher, S. Bourdarie, V. Maget, A. Sicard-Piet, G. Rolland and D. Standarovski, "High-Energy Electrons in the Inner Zone," in IEEE Transactions on Nuclear Science, vol. 65, no. 8, pp. 1546-1552, Aug. 2018.doi: 10.1109/TNS.2018.2824543.

[18] J. F. Fennell et al., "Van Allen Probes show that the inner radiation zone contains no MeV electrons: ECT/MagEIS data", Geophys. Res. Lett., vol. 42, no. 5, pp. 1283-1289, 2015.

[19] A. Sicard, D. Boscher, S. Bourdarie, D. Lazaro, D. Standarovski, and R. Ecoffet, “GREEN: the new Global Radiation Earth ENvironment model (beta version)”, Ann. Geophys., 36, 953-967, 2018.

[20] D. M. Sawyer and J. I. Vette, “AP-8 Trapped Proton Environment for Solar Maximum and Solar Minimum,” NSSDC WDC-A-R&S 76-06, 1976.

[21] J. I. Vette, “The NASA/National Space Science Data Center Trapped Radiation Environment Model Program (1964- 1991),” NSSDC/WDC-A-R&S 91-29, 1991.